

# Penetrating Electric Field Simulated by the MAGE and Observed by ICON

Qian Wu<sup>1</sup>, Wenbin Wang<sup>2</sup>, Dong Lin<sup>3</sup>, Chaosong Huang<sup>4</sup>, and Yongliang Zhang<sup>5</sup>

<sup>1</sup>National Center for Atmospheric Research (UCAR)

<sup>2</sup>HAO/NCAR

<sup>3</sup>National Center for Atmospheric Research

<sup>4</sup>Air Force Research Laboratory

<sup>5</sup>The Johns Hopkins University Applied Physics Laboratory

November 22, 2022

## Abstract

Using the newly developed, Multiscale Atmosphere-Geospace Environment (MAGE) model, we simulated the penetrating electric field in the equatorial region under different interplanetary magnetic field (IMF)  $B_z$  conditions during September 2020. Two intervals were selected for detailed analysis with the vertical ion drift data from the NASA ICON. The MAGE simulations show that in southward IMF (S-IMF) cases, the dawn-dusk electric potential drop at the equator is about 14% of the cross polar cap potential difference. The dawn-dusk potential drop at the equator varies instantaneously with the changes in the IMF  $B_z$  or interplanetary electric field, which in turn alters the vertical ion drift. The daytime changes of the equatorial vertical ion drift in response to the penetrating electric field related to the IMF  $B_z$  are only half of that during the nighttime, due mostly to the E-region dynamo. MAGE simulation shows pre-reversal enhancement (PRE) during southward IMF cases, but the PRE was absent in the ICON IVM observations. Further observations and modeling are needed to resolve this discrepancy.

## Introduction

Penetrating electric field is a high latitude dawn-dusk field applied to the mid and low latitudes at a much short time scale than thermosphere-ionosphere interaction process such as ion neutral collision. Penetration electric fields have been intensively studied in the past [e.g., Nishida, 1968; Kikuchi et al., 2008; W. Wang et al., 2008; Huang, 2019; Huang et al., 2005; Maruyama et al., 2005; Kelley et al., 2003; Fejer et al., 2007; Lu et al., 2012].

While the basic underlying physics is known, many aspects of the penetrating electric field (PEF) remain to be addressed. For example, it is difficult to simulate the penetrating electric field, which changes rapidly, using a first principle thermosphere and ionosphere model driven by empirical high latitude convection models such as *Heelis et al.* [1982] and *Weimer* [2005]. Lu et al. [2012] used the AMIE (Assimilative Mapping of Ionospheric Electrodynamics) [Richmond and Kamide, 1988] driven TIMEGCM (Thermosphere-Ionosphere-Mesosphere-Electrodynamical General Circulation Model) model to simulate penetrating electric field effects. While AMIE uses real data as inputs, the derived convection pattern at high latitudes still relies heavily on empirical data information. The case examined by Lu et al. [2012] was a very strong storm event (November 9-10, 2004), which produced 120 m/s vertical ion drift at the equator. High latitude model inputs with a high time resolution will enable the examination of the penetrating electric field in great details and improve the understanding of observed results, especially under weak to moderate geomagnetic activity conditions. One of the outstanding questions is how the penetration electric field is related to changes in the IMF  $B_z$

and the cross polar cap potential (CPCP). Penetrating electric field effect becomes complicated when the IMF Bz changes back and forth between northward and southward.

Towards the goal of better understanding the penetrating electric field, we use a coupled magnetosphere ionosphere model (MAGE, Multiscale Atmosphere-Geospace Environment) to simulate the penetrating electric field effect on the equatorial ionosphere [e.g., Lin et al., 2021; Pham et al., 2022], specifically on the vertical ion drift. The MAGE model provides much higher and more dynamic high latitude inputs of convection pattern and auroral precipitation by coupling with a magnetospheric model. The objective is to show how the IMF Bz component controls the equatorial vertical ion drift, through the CPCP and penetrating electric field. In addition to the latest modeling tools, we also will use the NASA ICON mission ion drift measurement to observe the effect of the penetrating electric field from an equatorial orbiting satellite platform. MAGE simulations are used to facilitate interpretation of the observational results.

We selected two geomagnetically active intervals during September 2020. The first interval is from September 24, 5-6 UT when the IMF Bz turned northward first and then turned southward within one hour, which is highlighted (blue shaded) in the IMF Bz and By subplot of Figure 1. The figure also includes solar wind speed and density, and the interplanetary electric field (IEF) dawn-dusk component. The IMF Bz variations led to changes in the IEF, which affects the dawn-dusk electric potential and penetrating electric field. The second interval is from September 26, 9-10 UT with the interval highlighted in Figure 2. In this case, IMF Bz turned southward within the highlighted interval. Moreover, we have ICON observations of the equatorial ExB meridional ion drift, which is upward at the magnetic dip equator, for comparison. The paper is organized by (1) a brief description of the model setup, (2) discussion of the simulation results for the two intervals, (3) comparison between the model results and ICON ion drift observations, and (4) additional discussion on the ICON ion drift data.

## Model Simulation Setup

The MAGE model [Pham et al., 2022; Lin et al., 2021] consists of the Grid Agnostic MHD with Extended Research Applications (GAMERA) model of the magnetosphere [Zhang et al. 2019], the Rice Convection Model (RCM) of the ring current [Toffoletto et al. 2003], the Thermospheric Ionosphere Electrodynamics General Circulation Model (TIEGCM) of the ionosphere-thermosphere [Richmond et al., 1992], and the RE-developed Magnetosphere-Ionosphere Coupler/Solver (REMIX) [Merkin and Lyon, 2010] that links different components of MAGE. As aforementioned, the standalone TIEGCM is traditionally driven by empirical high latitude ion convection models [e.g., Heelis et al. 1982; Weimer 2005] which simply use the three-hourly Kp index or selected solar wind parameters as inputs. These empirical models do not capture fast temporal variations of high latitude convection to address questions of the dynamic changes of global ionospheric electric fields, such as the penetrating electric field which can induce nearly instantaneous responses in the ionospheric thermospheric system in the equatorial region. In this study the magnetospheric model of GAMERA provides the dynamic features of electric potential at high latitudes for the TIEGCM at a cadence of every 10 s. Moreover, the MAGE model can resolve mesoscale convection structures such as subauroral polarization streams (SAPS) that are absent in the empirical models [Lin et al., 2021]. In addition, the MAGE also incorporates the RCM to simulate the ring current effect that can have implication for the penetrating electric field. It is also noted that the ring current may provide the shielding effect to the penetrating electric field. The model setup is shown in Figure 1 of Lin et al., [2021]. In this study, the MAGE model was driven by solar wind and IMF data obtained from the CDAWeb OMNI database with one-minute resolution. The simulated interval starts from 19 September 2020. Specifically, we focus on the TIEGCM outputs for the ionosphere-thermosphere, which have a spatial resolution of 1.25 degree latitudinally and longitudinally and 0.25 scale height vertically. The vertical direction consists of 57 grids spanning from the altitude of  $\sim 97$  km to  $\sim 600$  km. The time step is 5 seconds. We save the results every 5 minutes.

## ICON Observation

We also used the ion drift data from the NASA ICON mission [Immel et al., 2018] for a comparison with the MAGE simulation results. ICON is an equatorial mission for studying equatorial ionospheric connection to

the lower atmosphere. It carries ion velocity meter (IVM), which measure ion drift, density, and composition [Heelis et al., 2017]. In this study, we will only examine the IVM ExB meridional ion drift, which at the magnetic dip equator is vertically upward pointing. IVM ExB ion drifts are decomposed into magnetically zonal (horizontal, eastward is positive) and meridional (within the magnetic meridian plain, upward is positive). Hence, at the low latitudes, the meridional ion drift is a good approximation of the vertical ion drift. IVM samples the ion drift at 1 second cadence. The IVM data quality depends on the ion density. In our selected cases, we only used the data from noon to evening magnetic local time when the ion density is relatively high.

### MAGE Simulation for the Sep 24 05-06 UT Interval

We plot in Figure 3 the MAGE simulation results every 10 minutes over the 1-hour period. Six time intervals are highlighted by the cyan color. The IMF conditions are given in the top panel of Figure 3. The first interval is for the southward IMF condition (S-IMF) and followed by two northward IMF (N-IMF) intervals. Then a transition from northward to southward IMF (0-IMF) occurred and was followed by two southward IMF (S-IMF) intervals. The above changes in IMF Bz orientation provide an opportunity to examine how the IMF Bz component impacts the magnetosphere-ionosphere system from high to low latitudes. The IEF dawn-dusk component is also a good indicator for the ionospheric dawn-dusk potential, which determines the high latitude convection and penetrating electric field. IEF switched from positive to negative, then positive again in response to the changing sign of the IMF Bz.

The potential maps for the six IMF Bz conditions are shown in Figure 4a. All the variables from MAGE used in figures of this paper are selected from the pressure level 5.625 roughly at 405 km (the 50th vertical grid). The noon is on top of the plot and midnight at the bottom. The first image of an S-IMF case has a typical two-cell ion convection pattern with a CPCP of 84.7 kV at 0504 UT. In the second case (N-IMF at 0515 UT), the two-cell convection pattern remains but with a smaller CPCP of 51.2 kV. Even though the IMF turns northward, the anti-sunward convection within the polar cap remains probably due to the delay in the response of the nightside convection to changes in solar wind IMF conditions [e.g., Lu et al., 2002]. Only at 0525UT the second N-IMF case, a four-cell convection pattern appears with CPCP further reduced to 49.3 kV. The four-cell pattern is consistent with the N-IMF condition. The N-IMF case is followed by near zero IMF-Bz (0-IMF) at 0534UT when the four-cell pattern remains and the CPCP drops further to 37.4 kV. As soon as the IMF turns southward (S-IMF) at 0545 UT the two-cell convection pattern returns and CPCP increases to 105 kV. As the IMF remains southward (S-IMF) at 0555 UT, the two-cell pattern persists and the CPCP raises to 125 kV.

To illustrate how the penetrating electric field acts onto the low latitudes, we plot the same potential map for the entire northern hemisphere from the pole to the equator in Figure 4b. In the first case, the low latitude high potential is connected to the high latitude convection cell on the dawnside, which produces a potential drop from a morning peak and a nightside valley at the equator (7.5 kV). The yellow arrows indicate the electric fields on the dayside (eastward) and nightside (westward). In the second case at 0515 UT, the equatorial potential peak is on the dayside and the potential valley is on the nightside towards dawn with a potential drop  $\sim 6$  kV. It is noteworthy that there is no large dawn-dusk potential drop on either the dayside or nightside. The electric fields direct from noon to dawn and dusk and is very weak. The high latitude dawnside convection cell potential does not penetrate to the low latitudes. The same pattern persists at 0525 and 0534 UT as well. As IMF Bz turns southward (S-IMF), an equatorial potential peak occurs on the dawnside and a strong dawn-dusk potential drop is applied to the equatorial region ( $\sim 9$  kV) on both the dayside and nightside. To correlate the interplanetary electric field to the equatorial potential drop we list the values of these parameters in Table 1. We also plot these values in Figure 5. Because of the apparent correlation between the CPCP and the equatorial potential drop, we performed a linear fit between the CPCP and the equatorial potential drop shown on the rightside of Figure 5. The equatorial potential drop is about 14% of the CPCP.

**Table 1. IEF, CPCP, and Equatorial Potential**

Time (UT)	0504	0515	0525	0534	0545	0555
IEF (mV/m)	1.3	-3.3	-3.1	-0.4	2.2	3.3
CPCP (kV)	84.7	51.2	49.3	37.4	105	125
Equatorial Potential Drop (kV)	7.5	1.5	1.5	0.0	9.0	12

The nightside equatorial vertical ion drift response to the IMF Bz variations is shown in Figure 6a. In the background, the ionospheric F-region peak electron density (NmF2) is plotted. In the first S-IMF case at 0504 UT, the magnetic equatorial ion drift at night is large and downward. Towards the left (dusk), the model successfully simulates the Pre-Reversal Enhancement (PRE). The nighttime downward ion drift is consistent with the dawn-dusk potential (westward electric field) shown in Figure 4b. As soon as the IMF turns northward (N-IMF) at 0515 UT, the ion drift reduces and is close to zero (slightly upward), even though the two-cell convection still exists at high latitudes (Figure 4a). At 0525 UT during another N-IMF case, the ion drift is still close to zero but with an upward speed larger than that in the prior N-IMF case. In the next 0-IMF case at 0534 UT, the ion drift stays close to zero and with a smaller upward speed than the case earlier. As the southward IMF returns (S-IMF) at 0545 UT, the ion drift turns downward again. The ion drift stays downward during the same S-IMF case at 0555 UT in accordance with the strong westward electric field shown in Figure 4b.

The daytime variations of equatorial vertical ion drift are plotted in Figure 6b. Opposite to that in the nighttime, the daytime ion drift is mostly upward. In the first case of S-IMF at 0504 UT, there are relatively large upward ion drifts corresponding to a strong westward electric field (Figure 4b). As the IMF turns northward, the upward ion drift reduces by about 50% in the afternoon. In the morning, the ion drift reverses to downward. That is consistent with the dayside electric field displayed in Figure 4b, where the N-IMF case has dayside electric field westward in the morning and eastward in the afternoon. The same kind of configuration maintains until 0534 UT for both N-IMF and 0-IMF conditions. As the IMF turns southward (S-IMF) at 0545 UT, strong upward ion drifts appear at all dayside local times. The same configuration exists at 0555 UT (S-IMF) as well reflecting the strong eastward electric field (Figure 4b).

To make sure that we are seeing penetrating electric field, we need to examine the thermospheric zonal winds at the magnetic equator (Figure 7). If the ion drift variations shown in Figures 6a and 6b were not due to the penetrating electric field, they might be caused by thermospheric wind variations. Figure 7 shows almost unchanged neutral winds during the 09 to 10 UT time interval. That rules out the possibility of neutral wind dynamo causing the vertical ion drift variations in Figures 6a and 6b.

### MAGE Simulation and ICON IVM Observation for September 26, 09-10 UT Interval

We selected this interval because of the availability of the ICON ion drift data. Figure 8 shows the IMF and geomagnetic parameters in the 1-hour interval from 09 to 10 UT on September 26, 2021. We selected four intervals for analysis, which are highlighted. The first two are N-IMF cases followed by two S-IMF cases. Figure 9 shows the equatorial vertical ion drift during the four cases. In addition, we also plot the ICON ExB meridional drift in both magenta and cyan vectors from 09-10 UT. Note that ICON is a low-inclination satellite and takes ~50 minutes to fly over the dayside. In contrast, the simulated ion drifts are taken at a specific UT. Hence, the simulation match in the time only with a small portion of the plotted ICON data. To highlight that portion of observational match data, the magenta color represents the drifts from ICON at the same time as the model map plot. Just north of the ICON satellite track (at the bottom of the ICON drift vector) is the simulated ExB meridional ion drift from the MAGE plotted as a black line. The MAGE simulated ion drift is projected in the exact same direction as the definition of the IVM ExB meridional ion drift for an easy comparison. The vertical ion drift for the N-IMF and S-IMF cases are like those in Figure 6 during the daytime. During the S-IMF, there are strong upward ion drifts. Yet the ICON ion drifts show strong downward trend. Those ICON IVM ion drifts appear to have a large offset.

To address the issue, we calculated 6-min MLT median values from the day (orange line) and plot them with the raw 1 second data between 09 – 10 UT (green line) in Figure 10. As we can see that both raw data and

6-min MLT median values all show a downward drift at 18 MLT. The vertical ion drift reverses at 18 MLT in typical conditions [e.g. Aol et al., 2020], when we should expect zero vertical ion drift. After consulting with the IVM team from U. of Texas at Dallas, we applied a shift based on the 6-minute MLT median value at 18 MLT in the ExB meridional ion drift to bring the drift to zero at 18 MLT (blue line). We use the one-day 6-minute MLT median data for the shift to avoid any fast-oscillating effects of penetrating electric field on the correction.

We plot the corrected ICON ion drift in Figure 11. Comparing the simulated ExB ion drift along the ICON track with the corrected ICON IVM, we noticed significant differences. First, at earlier UT and MLT hours, the ICON IVM has stronger upward drift than the simulations at 0924 and 0935 UT. Unfortunately, when the S-IMF returns at 0945 UT, the ICON satellite was located close to 18 MLT when the ion drift is near zero. Hence, we could not see the strong upward ion drift measured by ICON (at earlier MLT hours), even though the model show enhancement. At 0954 UT, the IMF was still southward (S-IMF), the ICON satellite passed 18 MLT and entered the region where downward ion drift is expected. ICON IVM did indeed show downward (magenta vectors). However, the MAGE simulation shows a sizeable PRE in the ion drift, which ICON IVM did not see. Even the IVM data beyond 0954 UT in the cyan color did not show any signature of the PRE. There was no sign of PRE in the N-IMF cases in the simulation. The first sign of PRE appeared at 0945 UT during the first S-IMF case. It is possible that penetrating electric field during the N-IMF suppressed the PRE. We do notice that ICON did not see PRE during the S-IMF case whereas the model predicts one. We are still searching for the cause for the discrepancy on both the observation and simulation side.

## Discussion

### *High Latitude and Low Latitude Reaction to the IMF Bz Variation*

In the simulation of the September 24 05-06 UT case, the MAGE model simulated the penetrating electric field effect on the equatorial vertical ion drift. In the high latitudes, the MAGE magnetospheric input from GAMERA provides fast response to the varying IMF Bz conditions in convection pattern and CPCP. We noticed that the two-cell convection pattern does linger a bit as the IMF Bz turned northward at 0515 UT in Figure 4a, but its magnitude (CPCP) decreases compared with the southward IMF Bz case at the early UT. We note that in the daytime an extra convection cell already occurred in response to the northward turning of the IMF Bz. This is most likely related to the delay in the response of nightside convection to sudden solar wind and IMF condition changes [e.g., Lu et al., 2002]. While the high latitude nightside ion convection may have a longer memory, the equatorial electric field responds rapidly to high latitude convection changes. At 0515 UT, the strong downward ion drifts are gone on the nightside as well as the strong dawn-dusk potential near equator as shown Figure 6a. The dayside equatorial ion drifts also respond quickly at 0515 UT as shown in Figure 6b. Usually, one expects that the ion drifts at high latitudes react faster to changes in the solar wind and the magnetosphere. The simulation suggests that penetrating electric field acts on the equatorial region nearly instantaneously as shown in Figures 4b, 6a, and 6b. It appears that the ionospheric response to a S-IMF turning is a bit faster than a N-IMF turning at high latitudes depending on local time.

### *Penetrating Electric Field from the High Latitudes*

The MAGE also shows that during S-IMF cases, the dawnside high latitude convection cell is connected to the low latitude high potential point. During N-IMF, the convection cells are closed off from the low latitudes (Figure 4b). In the case of S-IMF more high latitude magnetic fields lines are open and linked to outside of the magnetosphere and the solar wind dynamo can act on larger latitudinal range and apply high dawn-dusk potential to the low latitudes. During the N-IMF case, the polar cap is smaller and open field lines are far away from the low latitude region.

### *Dayside/Nightside Differences*

Another point we should mention is the day/night difference in the equatorial ion drift reaction to the penetrating electric field. The nighttime vertical drift changes are twice as large as the daytime changes in

the opposite direction. That is likely due to the daytime E-region conductance influence. Further study is needed.

### *Link Penetrating Electric Field to the IEF*

Table 1 shows the links between the IEF, CPCP, and the equatorial dawn-dusk potential drop according to MAGE. When the IEF is positive, the equatorial dawn-dusk potential drop appears to be 14% of CPCP as shown in Figure 5. The IEF has larger relative increase than the CPCP and equatorial dawn-dusk potential in the MAGE model. That is understandable as the CPCP saturates near 100 kV when the IEF is above 3 mV/m [e.g., Shepherd et al., 2002]. MAGE model simulation appears to be consistent with that.

### *MAGE and ICON IVM Observation Comparison*

While we wish to see that ICON were able to observe the penetrating electric field effect directly, we could not find ICON data during the early afternoon hours when the IVM usually provides high quality data. We do notice that the ICON upward ion drifts in the morning hours were stronger than the MAGE simulation results. That suggests that the real equatorial dawn-dusk potential may be larger than that simulated by MAGE.

### *PRE Discrepancy*

One noticeable difference between the ICON IVM observation and MAGE simulation is the presence of the PRE in MAGE and absence in ICON IVM data. Right now, we do not have a definitive explanation for the discrepancy. The PRE in the MAGE simulations all occurred during the S-IMF cases. MAGE did not show any PRE during the N-IMF cases as the N-IMF condition induces downward vertical ion drift near the dusk. PRE is upward ion drift; hence N-IMF suppresses it.

### **Summary**

Using the MAGE model, we were able to show how the penetrating electric field varies with IMF Bz and is applied to the low latitudes. We summarize our findings as follows: 1. MAGE shows during the S-IMF cases, the dawn-dusk potential at the equator is about 1 tenth of the CPCP. 2. The dawn-dusk potential at the equator is applied instantaneously as the IMF Bz turns. 3. The daytime response of the equatorial vertical ion drift is about half of that during the nighttime, due probably to the E-region conductance influence. 4. MAGE simulation shows PRE during the S-IMF case, and PRE is absent in the ICON IVM observation. Further observations and modeling are needed to resolve this discrepancy.

### **Acknowledgement**

The work by Q.W. is supported by NASA grants 80NSSC20K0199, 80NAAC21K0014, NNX17AG69G and NSF grants AGS-2120511 and AGS-2054356. W.W. is supported by NASA grants 80NSSC17K0013, 80NSSC20K0601, 80NSSC20K0356, 80NSSC19K0080, 80NSSC17K0679, and 80NSSC20K0199. D.L. is supported by NASA grants 80NSSC17K0013, 80NSSC20K0601, 80NSSC21K0008, 80NSSC21K1677. C.H. is supported by NASA grants 80HQTR20T0015, 80HQTR20T0016, and NNN22OB17A. Y.Z. is supported by NASA grants 80NSSC20K0354 and 80NSSC21K1673. NCAR is supported by NSF. The ICON is a NASA mission, and the ion drift data can be obtained from [https://spdf.gsfc.nasa.gov/pub/data/icon/l2/l2-7\\_ivm-a/2020/](https://spdf.gsfc.nasa.gov/pub/data/icon/l2/l2-7_ivm-a/2020/) The MAGE simulation data used in this study are available from [https://gdex.ucar.edu/dataset/287\\_qwu.html](https://gdex.ucar.edu/dataset/287_qwu.html).

### **References**

- Aol, S., S. Buchert, E. Jurua, and M. Milla, Simultaneous ground-based and in-situ Swarm observations of equatorial F-region irregularities over Jicamarca, *Ann. Geophys.*, 38, doi: 10.5194/angeo-38-1063-2020.
- Fejer, B. G., J. W. Jensen, T. Kikuchi, M. A. Abdu, and J. L. Chau (2007), Equatorial ionospheric electric fields during the November 2004 magnetic storm, *J. Geophys. Res.*, 112, A10304, doi:10.1029/2007JA012376.

Pham, K. H., Zhang, B., Sorathia, K., Dang, T., Wang, W., Merkin, V., et al. (2022). Thermospheric density perturbations produced by traveling atmospheric disturbances during August 2005 storm. *Journal of Geophysical Research: Space Physics*, 127, e2021JA030071.

<https://doi.org/10.1029/2021JA030071>

Heelis, R. A., J. K. Lowell, and R. W. Spiro (1982), A model of the high latitude ionosphere convection pattern, *J. Geophys. Res.*, 87, 6339–6345, doi:10.1029/JA087iA08p06339.

Heelis, R.A., Stoneback, R.A., Perdue, M.D. et al. Ion Velocity Measurements for the Ionospheric Connections Explorer, *Space Sci Rev* **212**, 615–629 (2017). <https://doi.org/10.1007/s11214-017-0383-3>.

Huang, C.-S., J. C. Foster, and M. C. Kelley (2005), Long-duration penetration of the interplanetary electric field to the low-latitude ionosphere during the main phase of magnetic storms, *J. Geophys. Res.*, 110, A11309, doi:10.1029/2005JA011202.

Huang, C.-S. (2019), Long-lasting penetration electric fields during geomagnetic storms: Observations and mechanisms. *Journal of Geophysical Research: Space Physics*, 124. doi:10.1029/2019JA026793.

Immel et al., (2018), The Ionospheric connection explorer mission: Mission Goals and design, *Space Sci. Rev.*, doi:/10.1007/s11214-017-0449-2.

Kelley, M. C., J. J. Makela, J. L. Chau, and M. J. Nicolls (2003), Penetration of the solar wind electric field into the magnetosphere/ionosphere system, *Geophys. Res. Lett.*, 30 (4), 1158, doi:10.1029/2002GL016321.

Kikuchi, T., K. K. Hashimoto, and K. Nozaki (2008), Penetration of magnetospheric electric fields to the equator during a geomagnetic storm, *J. Geophys. Res.*, 113, A06214, doi:10.1029/2007JA012628.

Lin, D., Wang, W., Scales, W. A., Pham, K., Liu, J., Zhang, B., Maimaiti, M. (2019). Saps in the 17 March 2013 storm event: Initial results from the coupled magnetosphere-ionosphere-thermosphere model. *Journal of Geophysical Research: Space Physics*, 124(7), 6212–6225. doi: 10.1029/2019JA026698.

Lu, G., et al. (2002), Solar wind effects on ionospheric convection: A review, *J. Atmos. Sol. Terr. Phys.*, 64 (2), 145– 157. doi: 10.1016/S1364-6826(01)00080-3

Lu, G., L. Goncharenko, M. J. Nicolls, A. Maute, A. Coster, and L. J. Paxton (2012), Ionospheric and thermospheric variations associated with prompt penetration electric fields, *J. Geophys. Res.*, 117, A08312, doi:10.1029/2012JA017769.

Maruyama, N., A. D. Richmond, T. J. Fuller-Rowell, M. V. Codrescu, S. Sazykin, F. R. Toffoletto, R. W. Spiro, and G. H. Millward (2005), Interaction between direct penetration and disturbance dynamo electric fields in the storm-time equatorial ionosphere, *Geophys. Res. Lett.*, 32, L17105, doi:10.1029/2005GL023763.

Merkin, V., & Lyon, J. (2010). Effects of the low-latitude ionospheric boundary condition on the global magnetosphere. *Journal of Geophysical Research: Space Physics*, 115(A10). doi: 10.1029/2010JA015461.

Nishida, A. (1968), Coherence of geomagnetic *DP 2* fluctuations with interplanetary magnetic variations, *J. Geophys. Res.*, 73(17), 5549–5559, doi: 10.1029/JA073i017p05549.

Richmond, A., Ridley, E., & Roble, R. (1992). A thermosphere/ionosphere general circulation model with coupled electrodynamics. *Geophysical Research Letters*, 19(6), 601–604. doi: 10.1029/92GL00401.

Shepherd, S., Greenwald, R., & Ruohoniemi, J. (2002). Cross polar cap potentials measured with Super Dual Auroral Radar Network during quasi-steady solar wind and interplanetary magnetic field conditions. *Journal of Geophysical Research*, 107 (A7), 1094. <https://doi.org/10.1029/2001JA000152>.

Toffoletto, F., Sazykin, S., Spiro, R., & Wolf, R. (2003). Inner magnetospheric modeling with the rice convection model. *Space Science Reviews*, 107(1-2), 175– 196. doi: 10.1023/A:1025532008047.

Wang, W., J. Lei, A. G. Burns, M. Wiltberger, A. D. Richmond, S. C. Solomon, T. L. Killeen, E. R. Talaat, and D. N. Anderson (2008), Ionospheric electric field variations during a geomagnetic storm simulated by a coupled magnetosphere ionosphere thermosphere (CMIT) model, *Geophys. Res. Lett.* , *35* , L18105, doi:10.1029/2008GL035155.

Weimer, D. R. (2005), Improved ionospheric electrodynamic models and application to calculating Joule heating rates, *J. Geophys. Res. Space Physics* , *110* (A5), 1–21, doi:10.1029/2004JA010884.

Zhang, B., Sorathia, K. A., Lyon, J. G., Merkin, V. G., Garretson, J. S., & Wiltberger, M. (2019). GAMERA: A three-dimensional finite-volume MHD solver for non-orthogonal curvilinear geometries. *The Astrophysical Journal Supplement Series*, *244*(1), 20. doi: 10.3847/1538-4365/ab3a4c.

## Figures Captions

**Figure 1.** Interplanetary parameters during September 24, 2020. IMF Bz and By (first panel), solar wind speed (second panel), solar wind density (third panel) and interplanetary electric field (IEF) dawn-dusk component (forth panel). The time interval for detailed analysis is highlighted with cyan color from 05 to 06 UT, when the IMF Bz turned northward and southward.

**Figure 2.** Same as Figure 1 but for September 26, 2020.

**Figure 3.** Interplanetary parameters from September 24, 05-06 2020. The 6 samples represent S-IMF to N-IMF cases. For the S-IMF cases, the IEF dawn-dusk component is positive. During the N-IMF cases, the IEF is mostly negative.

**Figure 4a .** High latitude potential map during the September 24, 05-06, 2020. The noon is on the top and midnight at bottom. The equatorial boundary is at 40N. Dawn is on the right and dusk on the left. During the S-IMF cases, the two-cell convection pattern dominates. In case of N-IMF, the potential map shows multi-cell convection patterns. The Cross Polar Cap Potential (CPCP) is estimated based on the maximum and minimum values. The CPCP is much larger during the S-IMF than in the N-IMF cases.

**Figure 4b.** Same as Figure 5a but extended to the equator. By extending to the equator, the penetrating electric field effect to the equatorial region can be seen. The yellow arrows indicate the direction of the electric field during the S-IMF and N-IMF cases on the day and nightside of the equatorial region.

**Figure 5.** IEF, CPCP, and equatorial potential drop (dawn/dusk during S-IMF). Least squares fit for CPCP vs equatorial potential drop.

**Figure 6a.** Nightside vertical ion drift at the magnetic equator (black arrows downward drift shown as pointing southward in the figure) of September 24, 05-06 UT. Background is the nmf2 from the MAGE. Dusk is on the left. EIAs are clearly seen on the duskside. PRE is present in the first case. The vertical ion drift varies with IMF Bz component and equatorial electric field. During S-IMF cases, the vertical ion drifts are mostly downward. The scale vector is for 20 m/s.

**Figure 6b.** Same as Figure 6a but for dayside vertical ion drift. In most cases, the vertical ion drifts are upward.

**Figure 7.** The equatorial thermospheric zonal wind during September 24 05-06 UT at  $\sim 400$  km. The eastward zonal winds are positive shown as pointing northward with black vectors in the figure. The scale vector is for 20 m/s.

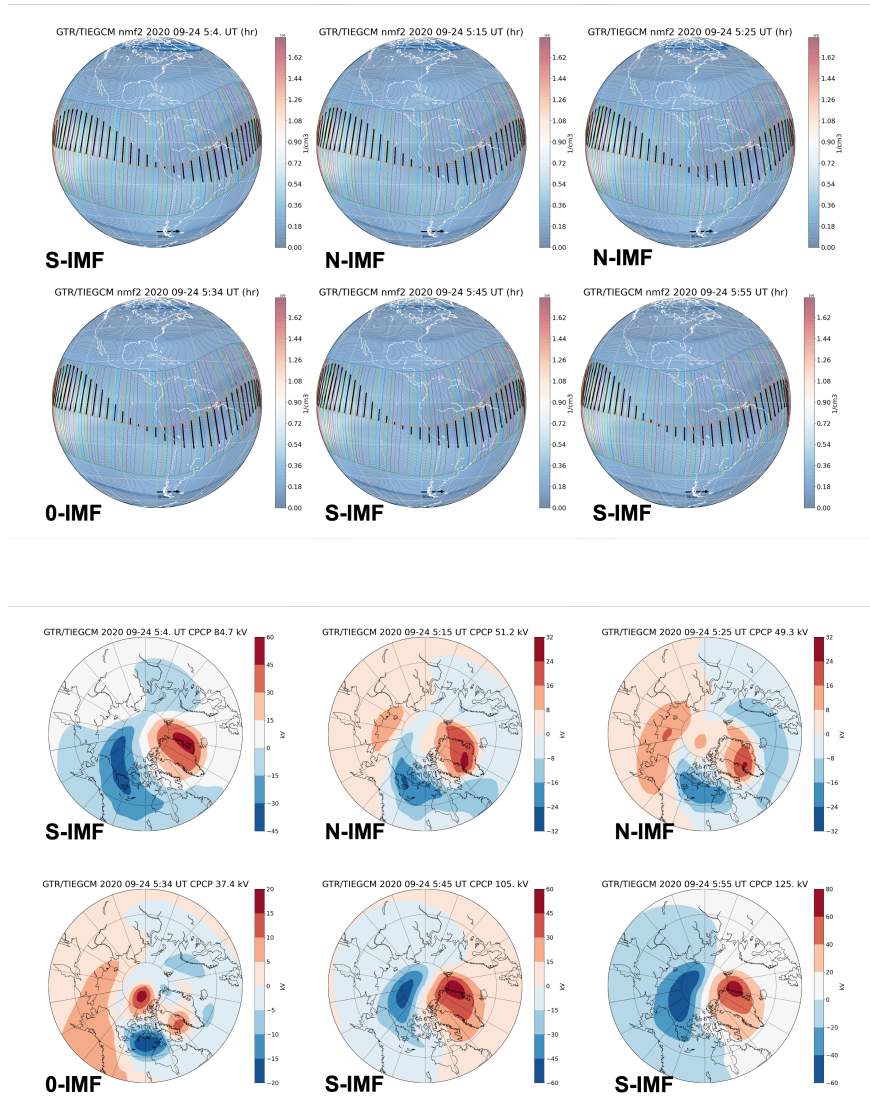
**Figure 8.** Interplanetary parameters for September 26, 09-10 UT in the same format as Figure 4.

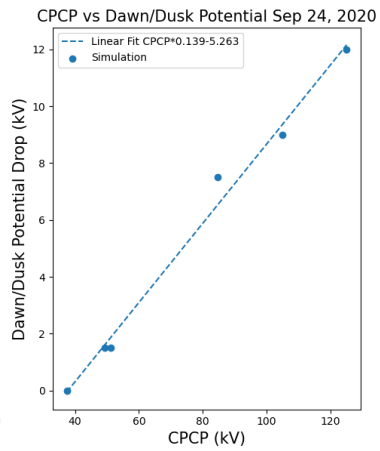
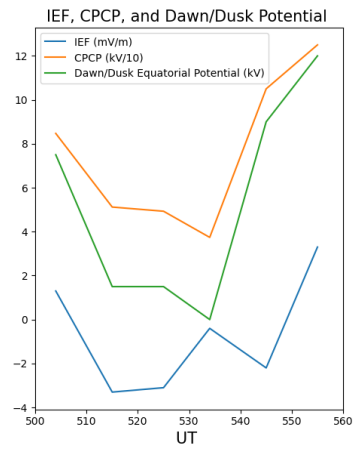
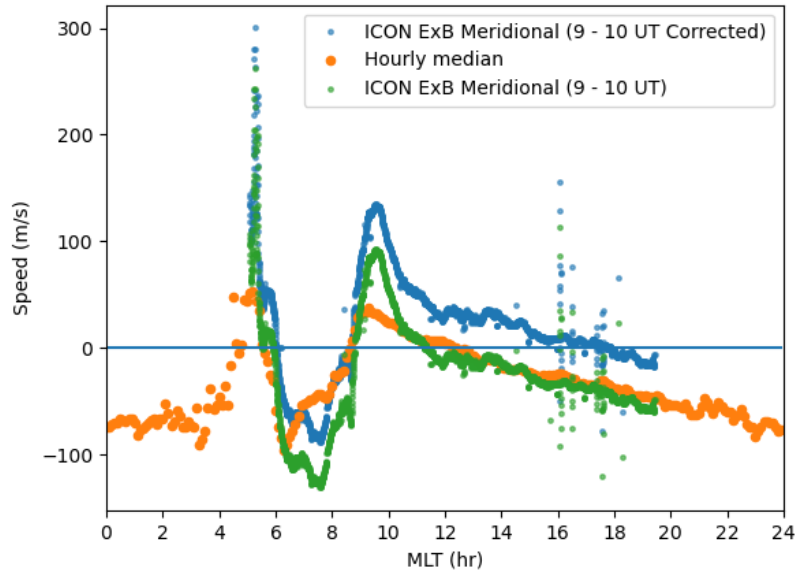
**Figure 9.** Comparison of the ICON ExB meridional ion drift (cyan and magenta vector lines from the ICON satellite track) with simulated ExB meridional ion drift (black line above the ICON satellite track) for September 26, 09-10 UT. The magenta vectors coincide with the time of the MAGE simulation for that particular subplot. As the ICON satellite cannot sample all spatial locations in the subplot simultaneously,

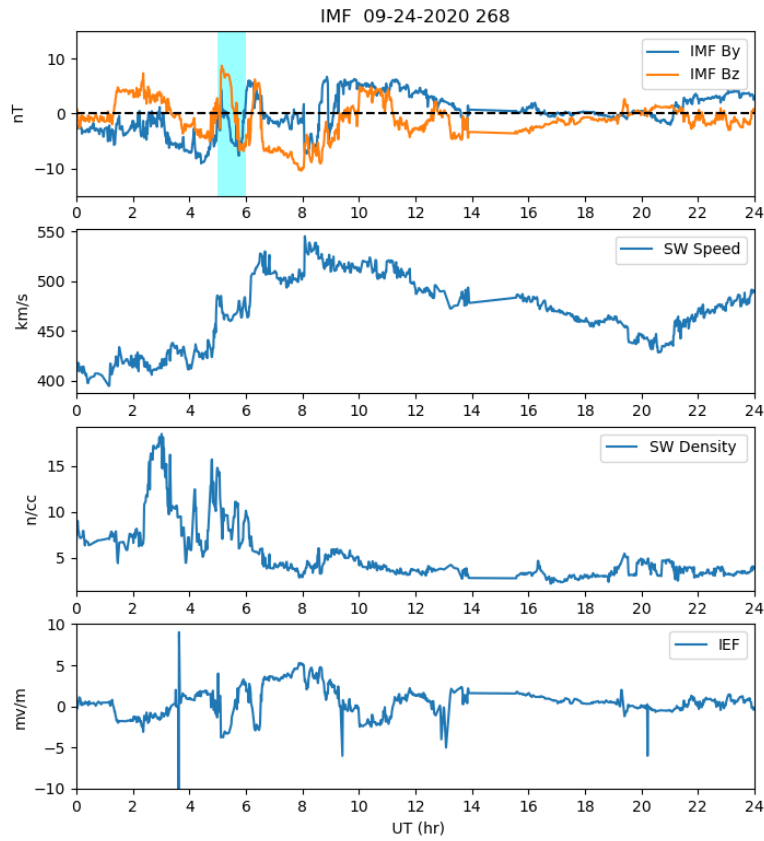
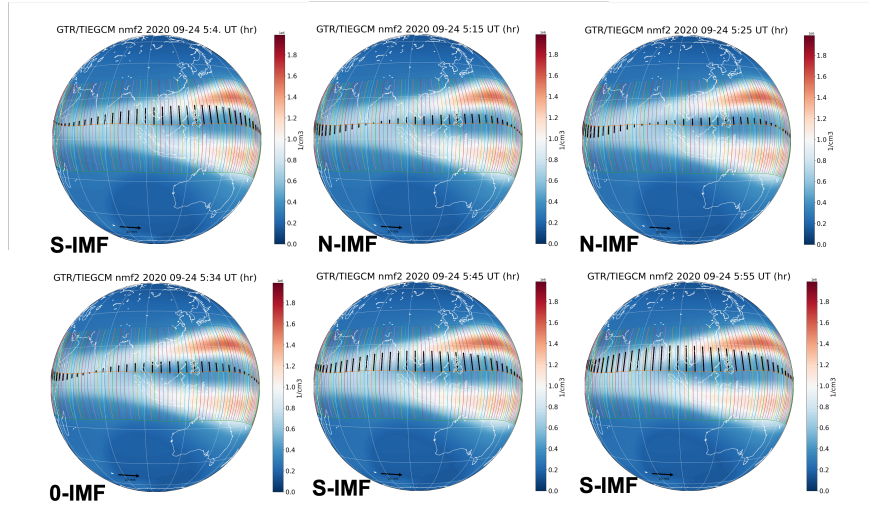
the satellite only measures a subsection for the section matching the time of simulation. The background is the nmf2. The equatorial vertical ion drift is shown as black vectors as in Figure 6b.

**Figure 10.** ICON IVM ExB meridional ion drift offset correction. The uncorrected IVM ion drift from 9-10 UT on Sep 26, 2020 (green) and daily magnetic local time hourly median values (orange). The 6-minute MLT median values have an offset of 37 m/s at 18 MLT, when the value on average should be zero. We use the 37 m/s offset corrected the IVM meridional ion drift (blue). The IVM data have issue with low ion density and photoelectron contamination before 12 MLT. Only the data after 12 MLT are used to compare with the model simulation.

**Figure 11.** Same as Figure 9, but for the corrected ICON IVM ExB meridional ion drift comparison with the model simulation.







# Penetrating Electric Field Simulated by the MAGE and Observed by ICON

Qian Wu<sup>1</sup>, Wenbin Wang<sup>1</sup>, Dong Lin<sup>1</sup>, Chaosong Huang<sup>2</sup>, and Yongliang Zhang<sup>3</sup>

<sup>1</sup>High Altitude Observatory, National Center for Atmospheric Research, Boulder, CO, USA

<sup>2</sup>Space Vehicles Directorate, Air Force Research Laboratory, Kirtland AFB, New Mexico, USA

<sup>3</sup>Applied Physics Laboratory, Johns Hopkins University, Laurel, MD, USA

## Abstract

Using the newly developed, Multiscale Atmosphere-Geospace Environment (MAGE) model, we simulated the penetrating electric field in the equatorial region under different interplanetary magnetic field (IMF) Bz conditions during September 2020. Two intervals were selected for detailed analysis with the vertical ion drift data from the NASA ICON. The MAGE simulations show that in southward IMF (S-IMF) cases, the dawn-dusk electric potential drop at the equator is about 14% of the cross polar cap potential difference. The dawn-dusk potential drop at the equator varies instantaneously with the changes in the IMF Bz or interplanetary electric field, which in turn alters the vertical ion drift. The daytime changes of the equatorial vertical ion drift in response to the penetrating electric field related to the IMF Bz are only half of that during the nighttime, due mostly to the E-region dynamo. MAGE simulation shows pre-reversal enhancement (PRE) during southward IMF cases, but the PRE was absent in the ICON IVM observations. Further observations and modeling are needed to resolve this discrepancy.

## Introduction

Penetrating electric field is a high latitude dawn-dusk field applied to the mid and low latitudes at a much short time scale than thermosphere-ionosphere interaction process such as ion neutral collision. Penetration electric fields have been intensively studied in the past [e.g., Nishida, 1968; Kikuchi et al., 2008; W. Wang et al., 2008; Huang, 2019; Huang et al., 2005; Maruyama et al., 2005; Kelley et al., 2003; Fejer et al., 2007; Lu et al, 2012].

While the basic underlying physics is known, many aspects of the penetrating electric field (PEF) remain to be addressed. For example, it is difficult to simulate the penetrating electric field, which changes rapidly, using a first principle thermosphere and ionosphere model driven by empirical high latitude convection models such as *Heelis et al.* [1982] and *Weimer* [2005]. Lu et al. [2012] used the AMIE (Assimilative Mapping of Ionospheric Electrodynamics) [Richmond and Kamide, 1988] driven TIMEGCM (Thermosphere-Ionosphere-Mesosphere-Electrodynamics General Circulation Model) model to simulate penetrating electric field effects. While AMIE uses real data as inputs, the derived convection

pattern at high latitudes still relies heavily on empirical data information. The case examined by Lu et al. [2012] was a very strong storm event (November 9-10, 2004), which produced 120 m/s vertical ion drift at the equator. High latitude model inputs with a high time resolution will enable the examination of the penetrating electric field in great details and improve the understanding of observed results, especially under weak to moderate geomagnetic activity conditions. One of the outstanding questions is how the penetration electric field is related to changes in the IMF Bz and the cross polar cap potential (CPCP). Penetrating electric field effect becomes complicated when the IMF Bz changes back and forth between northward and southward.

Towards the goal of better understanding the penetrating electric field, we use a coupled magnetosphere ionosphere model (MAGE, Multiscale Atmosphere-Geospace Environment) to simulate the penetrating electric field effect on the equatorial ionosphere [e.g., Lin et al., 2021; Pham et al., 2022], specifically on the vertical ion drift. The MAGE model provides much higher and more dynamic high latitude inputs of convection pattern and auroral precipitation by coupling with a magnetospheric model. The objective is to show how the IMF Bz component controls the equatorial vertical ion drift, through the CPCP and penetrating electric field. In addition to the latest modeling tools, we also will use the NASA ICON mission ion drift measurement to observe the effect of the penetrating electric field from an equatorial orbiting satellite platform. MAGE simulations are used to facilitate interpretation of the observational results.

We selected two geomagnetically active intervals during September 2020. The first interval is from September 24, 5-6 UT when the IMF Bz turned northward first and then turned southward within one hour, which is highlighted (blue shaded) in the IMF Bz and By subplot of Figure 1. The figure also includes solar wind speed and density, and the interplanetary electric field (IEF) dawn-dusk component. The IMF Bz variations led to changes in the IEF, which affects the dawn-dusk electric potential and penetrating electric field. The second interval is from September 26, 9-10 UT with the interval highlighted in Figure 2. In this case, IMF Bz turned southward within the highlighted interval. Moreover, we have ICON observations of the equatorial ExB meridional ion drift, which is upward at the magnetic dip equator, for comparison. The paper is organized by (1) a brief description of the model setup, (2) discussion of the simulation results for the two intervals, (3) comparison between the model results and ICON ion drift observations, and (4) additional discussion on the ICON ion drift data.

### **Model Simulation Setup**

The MAGE model [Pham et al., 2022; Lin et al., 2021] consists of the Grid Agnostic MHD with Extended Research Applications (GAMERA) model of the magnetosphere [Zhang et al. 2019], the Rice Convection Model (RCM) of the ring current [Toffoletto et al. 2003], the Thermospheric Ionosphere Electrodynamics General Circulation Model (TIEGCM) of the ionosphere-thermosphere [Richmond et al., 1992], and the RE-developed Magnetosphere-Ionosphere Coupler/Solver (REMIX) [Merkin and Lyon, 2010] that links different components

of MAGE. As aforementioned, the standalone TIEGCM is traditionally driven by empirical high latitude ion convection models [e.g., Heelis et al. 1982; Weimer 2005] which simply use the three-hourly Kp index or selected solar wind parameters as inputs. These empirical models do not capture fast temporal variations of high latitude convection to address questions of the dynamic changes of global ionospheric electric fields, such as the penetrating electric field which can induce nearly instantaneous responses in the ionospheric thermospheric system in the equatorial region. In this study the magnetospheric model of GAMERA provides the dynamic features of electric potential at high latitudes for the TIEGCM at a cadence of every 10 s. Moreover, the MAGE model can resolve mesoscale convection structures such as subauroral polarization streams (SAPS) that are absent in the empirical models [Lin et al., 2021]. In addition, the MAGE also incorporates the RCM to simulate the ring current effect that can have implication for the penetrating electric field. It is also noted that the ring current may provide the shielding effect to the penetrating electric field. The model setup is shown in Figure 1 of Lin et al., [2021]. In this study, the MAGE model was driven by solar wind and IMF data obtained from the CDAWeb OMNI database with one-minute resolution. The simulated interval starts from 19 September 2020. Specifically, we focus on the TIEGCM outputs for the ionosphere-thermosphere, which have a spatial resolution of 1.25 degree latitudinally and longitudinally and 0.25 scale height vertically. The vertical direction consists of 57 grids spanning from the altitude of  $\sim 97$  km to  $\sim 600$  km. The time step is 5 seconds. We save the results every 5 minutes.

### **ICON Observation**

We also used the ion drift data from the NASA ICON mission [Immel et al., 2018] for a comparison with the MAGE simulation results. ICON is an equatorial mission for studying equatorial ionospheric connection to the lower atmosphere. It carries ion velocity meter (IVM), which measure ion drift, density, and composition [Heelis et al., 2017]. In this study, we will only examine the IVM ExB meridional ion drift, which at the magnetic dip equator is vertically upward pointing. IVM ExB ion drifts are decomposed into magnetically zonal (horizontal, eastward is positive) and meridional (within the magnetic meridian plane, upward is positive). Hence, at the low latitudes, the meridional ion drift is a good approximation of the vertical ion drift. IVM samples the ion drift at 1 second cadence. The IVM data quality depends on the ion density. In our selected cases, we only used the data from noon to evening magnetic local time when the ion density is relatively high.

### **MAGE Simulation for the Sep 24 05-06 UT Interval**

We plot in Figure 3 the MAGE simulation results every 10 minutes over the 1-hour period. Six time intervals are highlighted by the cyan color. The IMF conditions are given in the top panel of Figure 3. The first interval is for the southward IMF condition (S-IMF) and followed by two northward IMF (N-IMF) intervals. Then a transition from northward to southward IMF (0-IMF) occurred and was followed by two southward IMF (S-IMF) intervals. The above

changes in IMF Bz orientation provide an opportunity to examine how the IMF Bz component impacts the magnetosphere-ionosphere system from high to low latitudes. The IEF dawn-dusk component is also a good indicator for the ionospheric dawn-dusk potential, which determines the high latitude convection and penetrating electric field. IEF switched from positive to negative, then positive again in response to the changing sign of the IMF Bz.

The potential maps for the six IMF Bz conditions are shown in Figure 4a. All the variables from MAGE used in figures of this paper are selected from the pressure level 5.625 roughly at 405 km (the 50th vertical grid). The noon is on top of the plot and midnight at the bottom. The first image of an S-IMF case has a typical two-cell ion convection pattern with a CPCP of 84.7 kV at 0504 UT. In the second case (N-IMF at 0515 UT), the two-cell convection pattern remains but with a smaller CPCP of 51.2 kV. Even though the IMF turns northward, the anti-sunward convection within the polar cap remains probably due to the delay in the response of the nightside convection to changes in solar wind IMF conditions [e.g., Lu et al., 2002]. Only at 0525 UT the second N-IMF case, a four-cell convection pattern appears with CPCP further reduced to 49.3 kV. The four-cell pattern is consistent with the N-IMF condition. The N-IMF case is followed by near zero IMF-Bz (0-IMF) at 0534 UT when the four-cell pattern remains and the CPCP drops further to 37.4 kV. As soon as the IMF turns southward (S-IMF) at 0545 UT the two-cell convection pattern returns and CPCP increases to 105 kV. As the IMF remains southward (S-IMF) at 0555 UT, the two-cell pattern persists and the CPCP raises to 125 kV.

To illustrate how the penetrating electric field acts onto the low latitudes, we plot the same potential map for the entire northern hemisphere from the pole to the equator in Figure 4b. In the first case, the low latitude high potential is connected to the high latitude convection cell on the dawnside, which produces a potential drop from a morning peak and a nightside valley at the equator (7.5 kV). The yellow arrows indicate the electric fields on the dayside (eastward) and nightside (westward). In the second case at 0515 UT, the equatorial potential peak is on the dayside and the potential valley is on the nightside towards dawn with a potential drop  $\sim 6$  kV. It is noteworthy that there is no large dawn-dusk potential drop on either the dayside or nightside. The electric fields direct from noon to dawn and dusk and is very weak. The high latitude dawnside convection cell potential does not penetrate to the low latitudes. The same pattern persists at 0525 and 0534 UT as well. As IMF Bz turns southward (S-IMF), an equatorial potential peak occurs on the dawnside and a strong dawn-dusk potential drop is applied to the equatorial region ( $\sim 9$  kV) on both the dayside and nightside. To correlate the interplanetary electric field to the equatorial potential drop we list the values of these parameters in Table 1. We also plot these values in Figure 5. Because of the apparent correlation between the CPCP and the equatorial potential drop, we performed a linear fit between the CPCP and the equatorial potential drop shown on the rightside of Figure 5. The equatorial potential drop is about 14% of the CPCP.

**Table 1. IEF, CPCP, and Equatorial Potential**

Time (UT)	0504	0515	0525	0534	0545	0555
IEF (mV/m)	1.3	-3.3	-3.1	-0.4	2.2	3.3
CPCP (kV)	84.7	51.2	49.3	37.4	105	125
Equatorial Potential Drop (kV)	7.5	1.5	1.5	0.0	9.0	12

The nightside equatorial vertical ion drift response to the IMF  $B_z$  variations is shown in Figure 6a. In the background, the ionospheric F-region peak electron density ( $NmF2$ ) is plotted. In the first S-IMF case at 0504 UT, the magnetic equatorial ion drift at night is large and downward. Towards the left (dusk), the model successfully simulates the Pre-Reversal Enhancement (PRE). The nighttime downward ion drift is consistent with the dawn-dusk potential (westward electric field) shown in Figure 4b. As soon as the IMF turns northward (N-IMF) at 0515 UT, the ion drift reduces and is close to zero (slightly upward), even though the two-cell convection still exists at high latitudes (Figure 4a). At 0525 UT during another N-IMF case, the ion drift is still close to zero but with an upward speed larger than that in the prior N-IMF case. In the next 0-IMF case at 0534 UT, the ion drift stays close to zero and with a smaller upward speed than the case earlier. As the southward IMF returns (S-IMF) at 0545 UT, the ion drift turns downward again. The ion drift stays downward during the same S-IMF case at 0555 UT in accordance with the strong westward electric field shown in Figure 4b.

The daytime variations of equatorial vertical ion drift are plotted in Figure 6b. Opposite to that in the nighttime, the daytime ion drift is mostly upward. In the first case of S-IMF at 0504 UT, there are relatively large upward ion drifts corresponding to a strong westward electric field (Figure 4b). As the IMF turns northward, the upward ion drift reduces by about 50% in the afternoon. In the morning, the ion drift reverses to downward. That is consistent with the dayside electric field displayed in Figure 4b, where the N-IMF case has dayside electric field westward in the morning and eastward in the afternoon. The same kind of configuration maintains until 0534 UT for both N-IMF and 0-IMF conditions. As the IMF turns southward (S-IMF) at 0545 UT, strong upward ion drifts appear at all dayside local times. The same configuration exists at 0555 UT (S-IMF) as well reflecting the strong eastward electric field (Figure 4b).

To make sure that we are seeing penetrating electric field, we need to examine the thermospheric zonal winds at the magnetic equator (Figure 7). If the ion drift variations shown in Figures 6a and 6b were not due to the penetrating electric field, they might be caused by thermospheric wind variations. Figure 7 shows almost unchanged neutral winds during the 09 to 10 UT time interval. That rules out the possibility of neutral wind dynamo causing the vertical ion drift variations in Figures 6a and 6b.

**MAGE Simulation and ICON IVM Observation for September 26,**

### 09-10 UT Interval

We selected this interval because of the availability of the ICON ion drift data. Figure 8 shows the IMF and geomagnetic parameters in the 1-hour interval from 09 to 10 UT on September 26, 2021. We selected four intervals for analysis, which are highlighted. The first two are N-IMF cases followed by two S-IMF cases. Figure 9 shows the equatorial vertical ion drift during the four cases. In addition, we also plot the ICON ExB meridional drift in both magenta and cyan vectors from 09-10 UT. Note that ICON is a low-inclination satellite and takes  $\sim 50$  minutes to fly over the dayside. In contrast, the simulated ion drifts are taken at a specific UT. Hence, the simulation match in the time only with a small portion of the plotted ICON data. To highlight that portion of observational data, the magenta color represents the drifts from ICON at the same time as the model map plot. Just north of the ICON satellite track (at the bottom of the ICON drift vector) is the simulated ExB meridional ion drift from the MAGE plotted as a black line. The MAGE simulated ion drift is projected in the exact same direction as the definition of the IVM ExB meridional ion drift for an easy comparison. The vertical ion drift for the N-IMF and S-IMF cases are like those in Figure 6 during the daytime. During the S-IMF, there are strong upward ion drifts. Yet the ICON ion drifts show strong downward trend. Those ICON IVM ion drifts appear to have a large offset.

To address the issue, we calculated 6-min MLT median values from the day (orange line) and plot them with the raw 1 second data between 09 – 10 UT (green line) in Figure 10. As we can see that both raw data and 6-min MLT median values all show a downward drift at 18 MLT. The vertical ion drift reverses at 18 MLT in typical conditions [e.g. Aol et al., 2020], when we should expect zero vertical ion drift. After consulting with the IVM team from U. of Texas at Dallas, we applied a shift based on the 6-minute MLT median value at 18 MLT in the ExB meridional ion drift to bring the drift to zero at 18 MLT (blue line). We use the one-day 6-minute MLT median data for the shift to avoid any fast-oscillating effects of penetrating electric field on the correction.

We plot the corrected ICON ion drift in Figure 11. Comparing the simulated ExB ion drift along the ICON track with the corrected ICON IVM, we noticed significant differences. First, at earlier UT and MLT hours, the ICON IVM has stronger upward drift than the simulations at 0924 and 0935 UT. Unfortunately, when the S-IMF returns at 0945 UT, the ICON satellite was located close to 18 MLT when the ion drift is near zero. Hence, we could not see the strong upward ion drift measured by ICON (at earlier MLT hours), even though the model show enhancement. At 0954 UT, the IMF was still southward (S-IMF), the ICON satellite passed 18 MLT and entered the region where downward ion drift is expected. ICON IVM did indeed show downward (magenta vectors). However, the MAGE simulation shows a sizeable PRE in the ion drift, which ICON IVM did not see. Even the IVM data beyond 0954 UT in the cyan color did not show any signature of the PRE. There was no sign of PRE in the N-IMF cases in the simulation. The first sign of PRE appeared at 0945 UT during the

first S-IMF case. It is possible that penetrating electric field during the N-IMF suppressed the PRE. We do notice that ICON did not see PRE during the S-IMF case whereas the model predicts one. We are still searching for the cause for the discrepancy on both the observation and simulation side.

## Discussion

### 1. *High Latitude and Low Latitude Reaction to the IMF Bz Variation*

In the simulation of the September 24 05-06 UT case, the MAGE model simulated the penetrating electric field effect on the equatorial vertical ion drift. In the high latitudes, the MAGE magnetospheric input from GAMERA provides fast response to the varying IMF Bz conditions in convection pattern and CPCP. We noticed that the two-cell convection pattern does linger a bit as the IMF Bz turned northward at 0515 UT in Figure 4a, but its magnitude (CPCP) decreases compared with the southward IMF Bz case at the early UT. We note that in the daytime an extra convection cell already occurred in response to the northward turning of the IMF Bz. This is most likely related to the delay in the response of nightside convection to sudden solar wind and IMF condition changes [e.g., Lu et al., 2002]. While the high latitude nightside ion convection may have a longer memory, the equatorial electric field responds rapidly to high latitude convection changes. At 0515 UT, the strong downward ion drifts are gone on the nightside as well as the strong dawn-dusk potential near equator as shown Figure 6a. The dayside equatorial ion drifts also respond quickly at 0515 UT as shown in Figure 6b. Usually, one expects that the ion drifts at high latitudes react faster to changes in the solar wind and the magnetosphere. The simulation suggests that penetrating electric field acts on the equatorial region nearly instantaneously as shown in Figures 4b, 6a, and 6b. It appears that the ionospheric response to a S-IMF turning is a bit faster than a N-IMF turning at high latitudes depending on local time.

### 1. *Penetrating Electric Field from the High Latitudes*

The MAGE also shows that during S-IMF cases, the dawnside high latitude convection cell is connected to the low latitude high potential point. During N-IMF, the convection cells are closed off from the low latitudes (Figure 4b). In the case of S-IMF more high latitude magnetic fields lines are open and linked to outside of the magnetosphere and the solar wind dynamo can act on larger latitudinal range and apply high dawn-dusk potential to the low latitudes. During the N-IMF case, the polar cap is smaller and open field lines are far away from the low latitude region.

### 1. *Dayside/Nightside Differences*

Another point we should mention is the day/night difference in the equatorial ion drift reaction to the penetrating electric field. The nighttime vertical drift changes are twice as large as the daytime changes in the opposite direction. That is likely due to the daytime E-region conductance influence. Further study is needed.

### 1. *Link Penetrating Electric Field to the IEF*

Table 1 shows the links between the IEF, CPCP, and the equatorial dawn-dusk potential drop according to MAGE. When the IEF is positive, the equatorial dawn-dusk potential drop appears to be 14% of CPCP as shown in Figure 5. The IEF has larger relative increase than the CPCP and equatorial dawn-dusk potential in the MAGE model. That is understandable as the CPCP saturates near 100 kV when the IEF is above 3 mV/m [e.g., Shepherd et al., 2002]. MAGE model simulation appears to be consistent with that.

### 1. *MAGE and ICON IVM Observation Comparison*

While we wish to see that ICON were able to observe the penetrating electric field effect directly, we could not find ICON data during the early afternoon hours when the IVM usually provides high quality data. We do notice that the ICON upward ion drifts in the morning hours were stronger than the MAGE simulation results. That suggests that the real equatorial dawn-dusk potential may be larger than that simulated by MAGE.

### 1. *PRE Discrepancy*

One noticeable difference between the ICON IVM observation and MAGE simulation is the presence of the PRE in MAGE and absence in ICON IVM data. Right now, we do not have a definitive explanation for the discrepancy. The PRE in the MAGE simulations all occurred during the S-IMF cases. MAGE did not show any PRE during the N-IMF cases as the N-IMF condition induces downward vertical ion drift near the dusk. PRE is upward ion drift; hence N-IMF suppresses it.

## **Summary**

Using the MAGE model, we were able to show how the penetrating electric field varies with IMF Bz and is applied to the low latitudes. We summarize our findings as follows: 1. MAGE shows during the S-IMF cases, the dawn-dusk potential at the equator is about 1 tenth of the CPCP. 2. The dawn-dusk potential at the equator is applied instantaneously as the IMF Bz turns. 3. The daytime response of the equatorial vertical ion drift is about half of that during the nighttime, due probably to the E-region conductance influence. 4. MAGE simulation shows PRE during the S-IMF case, and PRE is absent in the ICON IVM observation. Further observations and modeling are needed to resolve this discrepancy.

## **Acknowledgement**

The work by Q.W. is supported by NASA grants 80NSSC20K0199, 80NAAC21K0014, NNX17AG69G and NSF grants AGS-2120511 and AGS-2054356. W.W. is supported by NASA grants 80NSSC17K0013, 80NSSC20K0601, 80NSSC20K0356, 80NSSC19K0080, 80NSSC17K0679, and 80NSSC20K0199. D.L. is supported by NASA grants 80NSSC17K0013, 80NSSC20K0601, 80NSSC21K0008, 80NSSC21K1677. C.H. is supported by

NASA grants 80HQTR20T0015, 80HQTR20T0016, and NNN22OB17A. Y.Z. is supported by NASA grants 80NSSC20K0354 and 80NSSC21K1673. NCAR is supported by NSF. The ICON is a NASA mission, and the ion drift data can be obtained from [https://spdf.gsfc.nasa.gov/pub/data/icon/12/12-7\\_ivm-a/2020/](https://spdf.gsfc.nasa.gov/pub/data/icon/12/12-7_ivm-a/2020/) The MAGE simulation data used in this study are available from [https://gdex.ucar.edu/dataset/287\\_qwu.html](https://gdex.ucar.edu/dataset/287_qwu.html).

## References

- Aol, S., S. Buchert, E. Jurua, and M. Milla, Simultaneous ground-based and in-situ Swarm observations of equatorial F-region irregularities over Jicamarca, *Ann. Geophys.*, **38**, doi: 10.5194/angeo-38-1063-2020.
- Fejer, B. G., J. W. Jensen, T. Kikuchi, M. A. Abdu, and J. L. Chau (2007), Equatorial ionospheric electric fields during the November 2004 magnetic storm, *J. Geophys. Res.*, **112**, A10304, doi:10.1029/2007JA012376.
- Pham, K. H., Zhang, B., Sorathia, K., Dang, T., Wang, W., Merkin, V., et al. (2022). Thermospheric density perturbations produced by traveling atmospheric disturbances during August 2005 storm. *Journal of Geophysical Research: Space Physics*, **127**, e2021JA030071. <https://doi.org/10.1029/2021JA030071>
- Heelis, R. A., J. K. Lowell, and R. W. Spiro (1982), A model of the high latitude ionosphere convection pattern, *J. Geophys. Res.*, **87**, 6339–6345, doi:10.1029/JA087iA08p06339.
- Heelis, R.A., Stoneback, R.A., Perdue, M.D. *et al.* Ion Velocity Measurements for the Ionospheric Connections Explorer, *Space Sci Rev* **212**, 615–629 (2017). <https://doi.org/10.1007/s11214-017-0383-3>.
- Huang, C.-S., J. C. Foster, and M. C. Kelley (2005), Long-duration penetration of the interplanetary electric field to the low-latitude ionosphere during the main phase of magnetic storms, *J. Geophys. Res.*, **110**, A11309, doi:10.1029/2005JA011202.
- Huang, C.-S. (2019), Long-lasting penetration electric fields during geomagnetic storms: Observations and mechanisms. *Journal of Geophysical Research: Space Physics*, **124**. doi:10.1029/2019JA026793.
- Immel et al., (2018), The Ionospheric connection explorer mission: Mission Goals and design, *Space Sci. Rev.*, doi:/10.1007/s11214-017-0449-2.
- Kelley, M. C., J. J. Makela, J. L. Chau, and M. J. Nicolls (2003), Penetration of the solar wind electric field into the magnetosphere/ionosphere system, *Geophys. Res. Lett.*, **30**(4), 1158, doi:10.1029/2002GL016321.
- Kikuchi, T., K. K. Hashimoto, and K. Nozaki (2008), Penetration of magnetospheric electric fields to the equator during a geomagnetic storm, *J. Geophys. Res.*, **113**, A06214, doi:10.1029/2007JA012628.
- Lin, D., Wang, W., Scales, W. A., Pham, K., Liu, J., Zhang, B., Maimaiti, M. (2019). Saps in the 17 March 2013 storm event: Initial results from the cou-

- pled magnetosphere-ionosphere-thermosphere model. *Journal of Geophysical Research: Space Physics*, 124(7), 6212–6225. doi: 10.1029/2019JA026698.
- Lu, G., et al. (2002), Solar wind effects on ionospheric convection: A review, *J. Atmos. Sol. Terr. Phys.*, **64**(2), 145–157. doi: 10.1016/S1364-6826(01)00080-3
- Lu, G., L. Goncharenko, M. J. Nicolls, A. Maute, A. Coster, and L. J. Paxton (2012), Ionospheric and thermospheric variations associated with prompt penetration electric fields, *J. Geophys. Res.*, 117, A08312, doi:10.1029/2012JA017769.
- Maruyama, N., A. D. Richmond, T. J. Fuller-Rowell, M. V. Codrescu, S. Sazykin, F. R. Toffoletto, R. W. Spiro, and G. H. Millward (2005), Interaction between direct penetration and disturbance dynamo electric fields in the storm-time equatorial ionosphere, *Geophys. Res. Lett.*, *32*, L17105, doi:10.1029/2005GL023763.
- Merkin, V., & Lyon, J. (2010). Effects of the low-latitude ionospheric boundary condition on the global magnetosphere. *Journal of Geophysical Research: Space Physics*, 115(A10). doi: 10.1029/2010JA015461.
- Nishida, A. (1968), Coherence of geomagnetic *DP 2* fluctuations with interplanetary magnetic variations, *J. Geophys. Res.*, 73(17), 5549–5559, doi: 10.1029/JA073i017p05549.
- Richmond, A., Ridley, E., & Roble, R. (1992). A thermosphere/ionosphere general circulation model with coupled electrodynamics. *Geophysical Research Letters*, 19(6), 601–604. doi: 10.1029/92GL00401.
- Shepherd, S., Greenwald, R., & Ruohoniemi, J. (2002). Cross polar cap potentials measured with Super Dual Auroral Radar Network during quasi-steady solar wind and interplanetary magnetic field conditions. *Journal of Geophysical Research*, 107(A7), 1094. <https://doi.org/10.1029/2001JA000152>.
- Toffoletto, F., Sazykin, S., Spiro, R., & Wolf, R. (2003). Inner magnetospheric modeling with the rice convection model. *Space Science Reviews*, 107(1-2), 175–196. doi: 10.1023/A:1025532008047.
- Wang, W., J. Lei, A. G. Burns, M. Wiltberger, A. D. Richmond, S. C. Solomon, T. L. Killeen, E. R. Talaat, and D. N. Anderson (2008), Ionospheric electric field variations during a geomagnetic storm simulated by a coupled magnetosphere ionosphere thermosphere (CMIT) model, *Geophys. Res. Lett.*, *35*, L18105, doi:10.1029/2008GL035155.
- Weimer, D. R. (2005), Improved ionospheric electrodynamic models and application to calculating Joule heating rates, *J. Geophys. Res. Space Physics*, 110(A5), 1–21, doi:10.1029/2004JA010884.
- Zhang, B., Sorathia, K. A., Lyon, J. G., Merkin, V. G., Garretson, J. S., & Wiltberger, M. (2019). GAMERA: A three-dimensional finite-volume MHD

solver for non-orthogonal curvilinear geometries. The Astrophysical Journal Supplement Series, 244(1), 20. doi: 10.3847/1538-4365/ab3a4c.

### Figures Captions

**Figure 1.** Interplanetary parameters during September 24, 2020. IMF Bz and By (first panel), solar wind speed (second panel), solar wind density (third panel) and interplanetary electric field (IEF) dawn-dusk component (forth panel). The time interval for detailed analysis is highlighted with cyan color from 05 to 06 UT, when the IMF Bz turned northward and southward.

**Figure 2.** Same as Figure 1 but for September 26, 2920.

**Figure 3.** Interplanetary parameters from September 24, 05-06 2020. The 6 samples represent S-IMF to N-IMF cases. For the S-IMF cases, the IEF dawn-dusk component is positive. During the N-IMF cases, the IEF is mostly negative.

**Figure 4a.** High latitude potential map during the September 24, 05-06, 2020. The noon is on the top and midnight at bottom. The equatorial boundary is at 40N. Dawn is on the right and dusk on the left. During the S-IMF cases, the two-cell convection pattern dominates. In case of N-IMF, the potential map shows multi-cell convection patterns. The Cross Polar Cap Potential (CPCP) is estimated based on the maximum and minimum values. The CPCP is much larger during the S-IMF than in the N-IMF cases.

**Figure 4b.** Same as Figure 5a but extended to the equator. By extending to the equator, the penetrating electric field effect to the equatorial region can be seen. The yellow arrows indicate the direction of the electric field during the S-IMF and N-IMF cases on the day and nightside of the equatorial region.

**Figure 5.** IEF, CPCP, and equatorial potential drop (dawn/dusk during S-IMF). Least squares fit for CPCP vs equatorial potential drop.

**Figure 6a.** Nightside vertical ion drift at the magnetic equator (black arrows downward drift shown as pointing southward in the figure) of September 24, 05-06 UT. Background is the nmf2 from the MAGE. Dusk is on the left. EIAs are clearly seen on the duskside. PRE is present in the first case. The vertical ion drift varies with IMF Bz component and equatorial electric field. During S-IMF cases, the vertical ion drifts are mostly downward. The scale vector is for 20 m/s.

**Figure 6b.** Same as Figure 6a but for dayside vertical ion drift. In most cases, the vertical ion drifts are upward.

**Figure 7.** The equatorial thermospheric zonal wind during September 24 05-06 UT at  $\sim 400$  km. The eastward zonal winds are positive shown as pointing northward with black vectors in the figure. The scale vector is for 20 m/s.

**Figure 8.** Interplanetary parameters for September 26, 09-10 UT in the same format as Figure 4.

**Figure 9.** Comparison of the ICON ExB meridional ion drift (cyan and magenta vector lines from the ICON satellite track) with simulated ExB meridional ion drift (black line above the ICON satellite track) for September 26, 09-10 UT. The magenta vectors coincide with the time of the MAGE simulation for that particular subplot. As the ICON satellite cannot sample all spatial locations in the subplot simultaneously, the satellite only measures a subsection for the section matching the time of simulation. The background is the nmf2. The equatorial vertical ion drift is shown as black vectors as in Figure 6b.

**Figure 10.** ICON IVM ExB meridional ion drift offset correction. The uncorrected IVM ion drift from 9-10 UT on Sep 26, 2020 (green) and daily magnetic local time hourly median values (orange). The 6-minute MLT median values have an offset of 37 m/s at 18 MLT, when the value on average should be zero. We use the 37 m/s offset corrected the IVM meridional ion drift (blue). The IVM data have issue with low ion density and photoelectron contamination before 12 MLT. Only the data after 12 MLT are used to compare with the model simulation.

**Figure 11.** Same as Figure 9, but for the corrected ICON IVM ExB meridional ion drift comparison with the model simulation.